J. Appl. Comput. Mech., 8(2) (2022) 710-722
DOI: 10.22055/JACM.2021.39229.3377

ISSN: 2383-4536
jacm.scu.ac.ir

Shahid Chamran
University of Ahvaz

Journal of
Applied and Computational Mechanics

Research Paper

Effect of Porosity and Hygrothermal Environment on FGP Hollow Spheres under Electromechanical Loads

Rania Tantawy[1], Ashraf M. Zenkour[2]

[1] Department of Mathematics, Faculty of Science, Damietta University, P.O. Box 34517, Egypt, Email: rania_eltantwy@yahoo.com
[2] Department of Mathematics, Faculty of Science, Kafrelsheikh University, Kafrelsheikh 33516, Egypt, Email: zenkour@sci.kfs.edu.eg

Received November 19 2021; Revised December 24 2021; Accepted for publication December 24 2021.
Corresponding author: A.M. Zenkour (zenkour@sci.kfs.edu.eg)

Abstract. Semi-analytical studies for the porosity action of a hollow sphere made of functionally graded piezoelectric material are presented. A semi-analytical technique for radial displacement is presented. A combination of internal and external pressures, temperature distribution, uniform hygrothermal distribution, and an electric potential variation has been discussed between the inner and outer surfaces of the sphere. The material physical properties for the present porous hollow sphere are varying through the thickness due to the power functions of the radius. Numerical outcomes are validated for radial displacement, electric potential, and stresses for the perfect and porous functionally graded hollow sphere. The effect of different mechanical, piezoelectric, and hygrothermal are investigated.

Keywords: Porosity; Piezoelectric material; Functionally graded; Hygrothermal effect; Semi-analytical solution.

1. Introduction

Functionally graded piezoelectric materials (FGPMs) are kinds of piezoelectric materials with material composition and properties varying continuously in a certain direction. These new materials have a lot of applications in biomedical, aerospace, shipbuilding, dental implant medical implant and one more industry in modern engineering design [1]. Some papers referenced functionally graded piezoelectric porous material are introduced. For the first time, Wang *et al.* [2] studied the variation of longitudinally traveling FG porous material. Gupta and Talha [3] investigated the stability of FG porous plate with initial geometric imperfections. The vibration and sound radiation of FG porous plates with a temperature gradient through-thickness are presented by Zhou *et al.* [4] via the first-order shear deformation theory (FSDT). By using Hamilton's principle. Akbas [5] studied the mechanical properties of FG porous deep beams with different porosity models.

Several studies around the piezoelectric porous structure's characteristics are presented. Daikh and Zenkour [6] investigated the vibration and buckling of FG porous sandwich plates due to simple higher-order shear deformation theory (SHSDT). Zenkour *et al.* [7] are concerned with the buckling action of FGP porous plates employing a non-polynomial four-variable plate theory. Additional researchers have restricted their attention to porous structures [8-13].

Until now, a lot of articles concerned with the mechanical behavior of FGP models. Allam and Tantawy [14] displayed an analytical solution for hollow cylinders under loading of mechanical and electric potential. They examined their solution of viscoelastic isotropic hollow structures, strengthened by elastic isotropic fibers. The mechanical properties of FGMs are signified in the exponentially graded format [15-17] and power-law shape [18-23]. Additional reports of FGMs are found in the literature, such as Refs. [24-41].

This work is concerned with the porosity problem of a functionally graded piezoelectric hollow sphere. The composite sphere is subjected to a different combination of internal and external pressures, temperature distribution, uniform hygrothermal distribution effect, and an electric potential variation between the inner and outer surfaces of the sphere. The material physical properties for the present porous hollow sphere are varying through the thickness due to a refined power law. A semi-analytical technique is used to get the radial displacement and then to complete the solution. Some validation examples are investigated. Also, some outcomes are tabulated for future comparisons. Finally, the effects of different mechanical, piezoelectric, and hygrothermal parameters are discussed.

2. Mathematical Plan for FGP Porous Sphere

Let us investigate a functionally graded piezoelectric (FGP) porous hollow sphere composed of PZT-4 and Cadmium selenide. The properties of such materials are presented in Table 1 with perfect conductivity.

In this research, all material properties of the FGP porous sphere $P(r)$, along the radial direction are given by a polynomial function in the form

$$P(r) = \left(p^{(b)} - p^{(a)}\right)\left(\frac{r-a}{b-a}\right)^n + p^{(a)} - \frac{\beta}{2}\left(p^{(a)} + p^{(b)}\right), \tag{1}$$

where p_a and p_b are the inner and outer characteristic surfaces; a and b denote the inner and outer radii, respectively; $n \geq 0$ is the volume fraction exponent (n is a grading index) and $0 \leq \beta \leq 1$ is a porosity volume function.

Take the spherical coordinate of any point to be (r, θ, φ). The porous sphere loadings are denoted by temperature change $T(r)$, moisture distribution $C(r)$, and electric potential $\psi(r)$. Also, the porous sphere is supposed to radial displacement component $u(r)$ only and non-zero stresses $\sigma_i(r)$, and electric displacement $D_r(r)$. The constitutive relations are expressed as [42-44]

$$\begin{Bmatrix}\sigma_r\\ \sigma_\theta\end{Bmatrix} = \begin{bmatrix} c_{rr} & 2c_{r\theta} & e_{rr}\\ c_{r\theta} & c_{\theta\varphi} + c_{\theta\theta} & e_{r\theta}\end{bmatrix}\begin{Bmatrix}\frac{\mathrm{d}u}{\mathrm{d}r}\\ \frac{u}{r}\\ \frac{\mathrm{d}\psi}{\mathrm{d}r}\end{Bmatrix} - \begin{Bmatrix}\lambda_r\\ \lambda_\theta\end{Bmatrix}T(r) - \begin{Bmatrix}\eta_r\\ \eta_\theta\end{Bmatrix}C(r), \tag{2}$$

and

$$D_r = e_{rr}\frac{\mathrm{d}u}{\mathrm{d}r} + 2e_{r\theta}\frac{u}{r} - \varepsilon_{rr}\frac{\mathrm{d}\psi}{\mathrm{d}r} + p_{11}T(r) + p_{22}C(r), \tag{3}$$

where c_{ij} $(i = r, \theta, j = r, \theta, \varphi)$, e_{rj} $(j = r, \theta)$, ε_{rr}, p_{11}, p_{22} and $\eta_i (i = r, \theta)$ are elastic, piezoelectric, dielectric, pyroelectric, hygroelectric and moisture expansion coefficients, however λ_i take the forms

$$\begin{Bmatrix}\lambda_r\\ \lambda_\theta\end{Bmatrix} = \begin{bmatrix} c_{rr} & 2c_{r\theta}\\ c_{r\theta} & c_{\theta\varphi} + c_{\theta\theta}\end{bmatrix}\begin{Bmatrix}\alpha_r\\ \alpha_\theta\end{Bmatrix}, \tag{4}$$

in which α_i are the thermal expansion constants. Mainly, the survey assumes that c_{ij} $(i, j = r, \theta, \varphi)$, e_{rj}, α_i, p_{11} and p_{22} of the porous sphere follow the gradation relation in Eq. (1).

3. Governing Equations

3.1 Heat equation

The temperature change equation of the porous sphere is given along the heat conduction equation

$$\frac{1}{r}\frac{\mathrm{d}}{\mathrm{d}r}\left(Kr\frac{\mathrm{d}T(r)}{\mathrm{d}r}\right) + q(r) = 0, \tag{5}$$

where K is heat conductivity constant and $q(r)$ is the heat source function.

The temperature is produced at a situation-dependent rate contained by the inner surface and it moves to the outer surface, while the outer surface is temperature-free (insulated). The boundary conditions for temperature are expressed as

$$T(r)|_{r=a} = T_0, \qquad \left.\frac{\mathrm{d}T(r)}{\mathrm{d}r}\right|_{r=b} = 0, \tag{6}$$

where T_0 is reference primary temperature. The heat source surrounded by the inner and outer surfaces is explained by the heat conduction generating function

$$q(r) = \frac{Q}{ab}(r-a)(b-r), \quad a \leq r \leq b, \tag{7}$$

where Q represents the heat constant. By integrating Eq. (5) twice, one can solve the heat conduction equation as

$$T(r) = \frac{Qr^2}{144Kab}[9(r^2 + 4ab) - 16r(a+b)] + c_1\ln(r) + c_2, \tag{8}$$

in which c_1 and c_2 represent integration constants. They determined by applying the boundary conditions specified in Eq. (6), in the form

$$\left.\begin{aligned} c_1 &= \frac{Qb^2}{12\kappa a}(b-2a),\\ c_2 &= \frac{Q}{144Kab}[a^3(7a-20b) - 12b^3\ln(a)(b-2a)] + T_0.\end{aligned}\right\} \tag{9}$$

3.2 Moisture Propagation Equation

The physical form of the moisture diffusion equation is like the heat conduction equation. In porous hollow sphere, it can be described by Fickian moisture diffusion [45] as:

$$\frac{1}{r}\frac{\mathrm{d}}{\mathrm{d}r}\left(r\frac{\mathrm{d}C(r)}{\mathrm{d}r}\right) = 0. \tag{10}$$

The solution procedure of Eq. (6), is

$$C(r) = c_3\ln(r) + c_4, \tag{11}$$

where c_3 and c_4 are integration constants. The boundary conditions for the moisture diffusion are expressed as

$$C(r)|_{r=a} = 0, \qquad C(r)|_{r=b} = C_0, \tag{12}$$

where C_0 denotes the initial moisture concentration. So, the other constants c_3 and c_4 are equal to

$$c_3 = \frac{C_0}{\ln(b)-\ln(a)}, \qquad c_4 = -\frac{C_0\ln(a)}{\ln(b)-\ln(a)}. \tag{13}$$

3.3 Equilibrium Equations

The equilibrium and Maxwell equations of the FGP porous hollow sphere in one dimension in the absence of body force and electric charge intensity are [46]:

$$\frac{\mathrm{d}\sigma_r}{\mathrm{d}r} + \frac{2(\sigma_r - \sigma_\theta)}{r} = 0, \tag{14}$$

$$\frac{\mathrm{d}D_r}{\mathrm{d}r} + \frac{2D_r}{r} = 0. \tag{15}$$

4. Elastic Process for the Porous Sphere

The closed-form solution for the FGP porous sphere is obtained by solving temperature and moisture equations firstly, then solving equilibrium and Maxwell's equations together with the set of boundary conditions on the porous sphere.

The solution of temperature and moisture equations are described in Eqs. (8) and (11), respectively, and the solution of electric displacement appeared in Eq. (15) is expressed in the form

$$D_r = \frac{A_1}{r^2}, \tag{16}$$

where A_1 represents a new undefined constant. Then, Eqs. (3) and (16) with the assistance of polynomial relation appeared in Eq. (1), gives

$$\frac{\mathrm{d}\psi}{\mathrm{d}r} = \frac{1}{\varepsilon_{rr}}\left(e_{rr}\frac{\mathrm{d}u}{\mathrm{d}r} + 2e_{r\theta}\frac{u}{r} + p_{11}T(r) + p_{22}C(r) - \frac{A_1}{r^2}\right). \tag{17}$$

The controlling ordinary differential equation, Eq. (14), of radial displacement in terms of temperature, moisture, and electric displacement can be summarized as

$$\begin{gathered}\frac{\mathrm{d}^2u}{\mathrm{d}r^2} + \left(\frac{2}{r} + \frac{1}{m_{11}}\frac{\mathrm{d}m_{11}}{\mathrm{d}r}\right)\frac{\mathrm{d}u}{\mathrm{d}r} + \frac{2}{rm_{11}}\left(\frac{\mathrm{d}m_{12}}{\mathrm{d}r} + \frac{m_{12}-m_{22}}{r}\right)u + \frac{m_{41}}{m_{11}}\frac{\mathrm{d}C}{\mathrm{d}r} + \frac{1}{m_{11}}\left(\frac{\mathrm{d}m_{41}}{\mathrm{d}r} + \frac{2(m_{41}-m_{42})}{r}\right)C(r) \\ + \frac{m_{31}}{m_{11}}\frac{\mathrm{d}T}{\mathrm{d}r} + \frac{1}{m_{11}}\left(\frac{\mathrm{d}m_{31}}{\mathrm{d}r} + \frac{2(m_{31}-m_{32})}{r}\right)T(r) - \frac{1}{r^2m_{11}}\left(\frac{\mathrm{d}m_{51}}{\mathrm{d}r} - \frac{2m_{52}}{r}\right)A_1 = 0,\end{gathered} \tag{18}$$

where m_{ij} are functions of r

$$\left.\begin{array}{lll} m_{11} = c_{rr} + \dfrac{e_{rr}^2}{\varepsilon_{rr}}, & m_{12} = c_{r\theta} + \dfrac{e_{rr}e_{r\theta}}{\varepsilon_{rr}}, & m_{22} = c_{\theta\varphi} + c_{\theta\theta} + 2\dfrac{e_{r\theta}^2}{\varepsilon_{rr}}, \\ m_{31} = \dfrac{e_{rr}p_{11}}{\varepsilon_{rr}} - \lambda_r, & m_{32} = \dfrac{e_{r\theta}p_{11}}{\varepsilon_{rr}} - \lambda_\theta, & m_{41} = \dfrac{e_{rr}p_{22}}{\varepsilon_{rr}} - \eta_r, \\ m_{42} = \dfrac{e_{r\theta}p_{22}}{\varepsilon_{rr}} - \eta_\theta, & m_{51} = \dfrac{e_{rr}}{\varepsilon_{rr}}, & m_{52} = \dfrac{e_{r\theta}}{\varepsilon_{rr}}, \end{array}\right\}. \tag{19}$$

So, the full solution to the displacement u may be utilized to achieve the electric potential. Integrating Eq. (17) provides the electric potential $\psi(r)$ with further arbitrary integration constant A_2.

Now, the mechanical boundary conditions of the porous sphere may be represented by

$$\sigma_r|_{r=a} = -P_1, \quad \sigma_r|_{r=b} = -P_2. \tag{20}$$

where P_1 and P_2 denote the pressures on inner and outer surfaces, respectively. Finally, the constants A_1 and A_2 are specified by applying the electric boundary conditions

$$\psi(r)|_{r=a} = \psi_1, \quad \psi(r)|_{r=b} = \psi_2. \tag{21}$$

The complete solution of Eq. (18) as a function of variable r is very complicated. So, it is appropriate to use a semi-analytical solution to solve Eq. (18). In this technique, the porous sphere radial domain should be split into some virtual sub-domains with wideness $s^{(k)}$, as shown in Fig. 1. Evaluating the factors of Eq. (18) at $r = r^{(k)}$, the mean radius of the kth split, and using them instead of variable coefficients in Eq. (18), that is

$$\frac{\mathrm{d}^2u^{(k)}}{\mathrm{d}r^2} + N_1^{(k)}\frac{\mathrm{d}u^{(k)}}{\mathrm{d}r} + N_2^{(k)}u^{(k)} - N_3^{(k)} = 0, \tag{22}$$

where

$$N_1^{(k)} = \frac{2}{r^{(k)}} + \frac{1}{m_{11}(r^{(k)})}\left.\frac{\mathrm{d}m_{11}}{\mathrm{d}r}\right|_{r=r^{(k)}},$$

$$N_2^{(k)} = \frac{2}{r^{(k)}m_{11}(r^{(k)})}\left(\left.\frac{\mathrm{d}m_{12}}{\mathrm{d}r}\right|_{r=r^{(k)}} + \frac{m_{12}(r^{(k)}) - m_{22}(r^{(k)})}{r^{(k)}}\right),$$

$$\begin{aligned}N_3^{(k)} = &-\frac{m_{41}(r^{(k)})}{m_{11}(r^{(k)})}\left.\frac{\mathrm{d}C}{\mathrm{d}r}\right|_{r=r^{(k)}} - \frac{m_{31}(r^{(k)})}{m_{11}(r^{(k)})}\left.\frac{\mathrm{d}T}{\mathrm{d}r}\right|_{r=r^{(k)}} - \frac{1}{m_{11}(r^{(k)})}\left(\left.\frac{\mathrm{d}m_{41}}{\mathrm{d}r}\right|_{r=r^{(k)}} + \frac{2\left(m_{41}(r^{(k)}) - m_{42}(r^{(k)})\right)}{r^{(k)}}\right)C(r^{(k)}) \\ &-\frac{1}{m_{11}(r^{(k)})}\left(\left.\frac{\mathrm{d}m_{31}}{\mathrm{d}r}\right|_{r=r^{(k)}} + \frac{2\left(m_{31}(r^{(k)}) - m_{32}(r^{(k)})\right)}{r^{(k)}}\right)T(r^{(k)}) + \frac{1}{(r^{(k)})^2m_{11}(r^{(k)})}\left(\left.\frac{\mathrm{d}m_{51}}{\mathrm{d}r}\right|_{r=r^{(k)}} - \frac{2m_{52}(r^{(k)})}{r^{(k)}}\right)A_1^{(k)},\end{aligned}$$

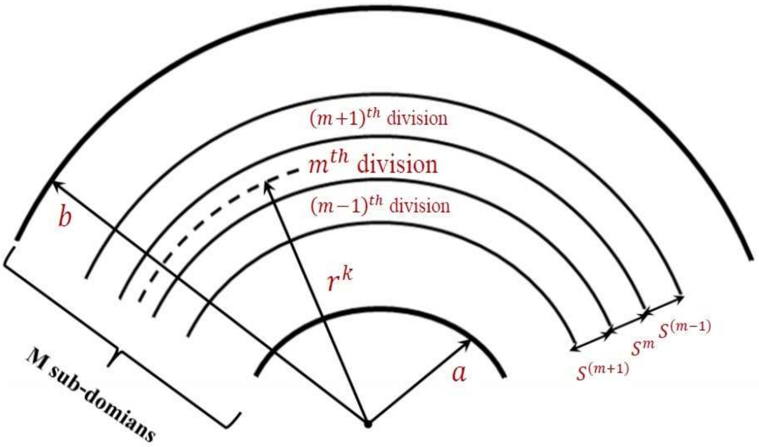

Fig. 1. Dividing radial domain into some finite sub-domain.

in which m_{ij} are given in terms of $r^{(k)}$. Utilizing the above methodology, Eq. (18) with variable coefficients is varied into a system of m differential equations with constant terms and m is being the number of virtual sub-domains. So, we obtain the displacement by solving Eq. (22) concerning r in the form

$$u^{(k)} = B_1^{(k)} e^{\delta_1 r} + B_2^{(k)} e^{\delta_2 r} + \frac{N_3^{(k)}}{N_2^{(2)}}, \tag{23}$$

where δ_1, δ_2 are the roots of the equation $\delta^2 + N_1^{(k)}\delta + N_2^{(k)} = 0$, and $\mathrm{B}_1^{(k)}$ and $\mathrm{B}_2^{(k)}$are differential constants for kth sub-domain. Also, the solution of Eq. (22) is applicable for

$$r^{(k)} - \frac{s^{(k)}}{2} \leq r \leq r^{(k)} + \frac{s^{(k)}}{2},$$

where $r^{(k)}$ and $s^{(k)}$ denote the mean radius and the radial width of the kth sub-domain, respectively. The differential equation constants $\mathrm{B}_1^{(k)}$ and $\mathrm{B}_2^{(k)}$ determined from the continuity conditions between every two adjacent sub-domains. So, the continuity conditions of the radial displacement, stresses, and electric potential distribution are required at the interfaces of the adjacent sub-domains in the form

$$\begin{aligned} u^{(k)}\Big|_{r=r^{(k)}+\frac{s^{(k)}}{2}} &= u^{(k+1)}\Big|_{r=r^{(k+1)}-\frac{s^{(k+1)}}{2}}, \\ \sigma_r^{(k)}\Big|_{r=r^{(k)}+\frac{s^{(k)}}{2}} &= \sigma_r^{(k+1)}\Big|_{r=r^{(k+1)}-\frac{s^{(k+1)}}{2}}, \\ \psi^{(k)}\Big|_{r=r^{(k)}+\frac{s^{(k)}}{2}} &= \psi^{(k+1)}\Big|_{r=r^{(k+1)}-\frac{s^{(k+1)}}{2}}. \end{aligned} \tag{24}$$

The continuity equations appeared in Eqs. (24), altogether with elastic and electric boundary conditions, Eqs. (20) and (21), give a collection of linear algebraic equations in $A_{1,k}$, $A_{2,k}$, $B_{1,k}$, $B_{2,k}$, $(k = 1,2, \dots, m)$. Solving these equations and substituting them in Eqs. (23), the displacements $u^{(k)}$ are established in each sub-domain. Increasing the number of divisions develops the reliability of the results.

5. Numerical Results and Discussion

Numerical outcomes for FGP porous spheres are displayed. The porous sphere is under pressure and electric potential in four different cases of boundary conditions. The dimensionless displacement, stresses, and electric potential will be given according to the case study.

In mathematical calculations, the material properties of PZT-4 (inner surface) and Cadmium selenide (outer surface) are considered in Table 1 [47, 48]. In extension, the amount of heat source $Q = 12$ (W/m^3) and the thermal conductivity factor $K = 0.35$ (W/Km). We take the inner and outer radii of the porous sphere $a = 0.2$ (m) and $b = 1$ (m).

Table 1. Material properties for PZT-4 and Cadmium selenide.

PZT-4 [47]	Cadmium selenide [48]
$c_{rr}^{(a)} = 115 \times 10^9$ (Pa)	$c_{rr}^{(b)} = 83.6 \times 10^9$ (Pa)
$c_{r\theta}^{(a)} = 74.3 \times 10^9$ (Pa)	$c_{r\theta}^{(b)} = 39.3 \times 10^9$ (Pa)
$c_{\theta\varphi}^{(a)} = 77.8 \times 10^9$ (Pa)	$c_{\theta\varphi}^{(b)} = 45.2 \times 10^9$ (Pa)
$c_{\theta\theta}^{(a)} = 139 \times 10^9$ (Pa)	$c_{\theta\theta}^{(b)} = 74.1 \times 10^9$ (Pa)
$e_{rr}^{(a)} = 15.1$ (Cm^{-2})	$e_{rr}^{(b)} = 0.347$ (Cm^{-2})
$e_{r\theta}^{(a)} = -5.2$ (Cm^{-2})	$e_{r\theta}^{(b)} = 0.16$ (Cm^{-2})
$\varepsilon_{rr}^{(a)} = 3.87 \times 10^{-9}$ (C^{2}K^{-1}m^2)	$\varepsilon_{rr}^{(b)} = 9.03 \times 10^{-11}$ (C^{2}K^{-1}m^2)
$p_{11}^{(a)} = -2.5 \times 10^{-5}$ (CK^{-1}m^{-2})	$p_{11}^{(b)} = -2.94 \times 10^{-6}$ (CK^{-1}m^{-2})
$\alpha_r^{(a)} = 2 \times 10^{-5}$ (K^{-1})	$\alpha_r^{(b)} = 2.458 \times 10^{-6}$ (K^{-1})
$\alpha_\theta^{(a)} = 2 \times 10^{-6}$ (K^{-1})	$\alpha_\theta^{(b)} = 4.396 \times 10^{-6}$ (K^{-1})
$\eta_r^{(a)} = 0.03 \times c_{rr}^{(a)}$ (m^{3}kg^{-1}Pa)	$\eta_r^{(b)} = 0.03 \times c_{rr}^{(b)}$ (m^{3}kg^{-1}Pa)
$\eta_\theta^{(a)} = 0$ (m^{3}kg^{-1}Pa)	$\eta_\theta^{(b)} = 0$ (m^{3}kg^{-1}Pa)

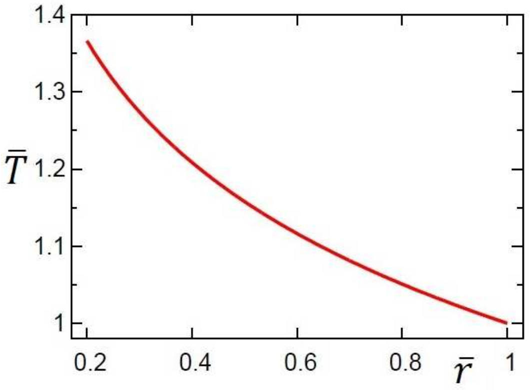

Fig. 2. Temperature distribution in EGP hollow sphere.

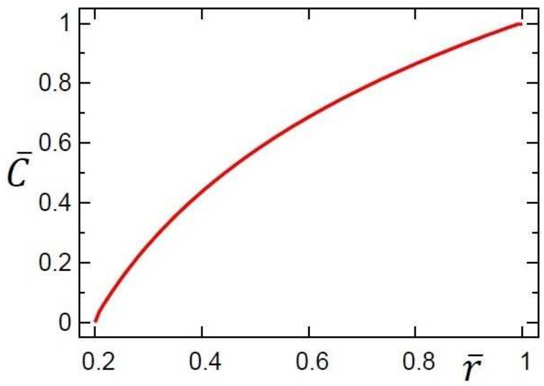

Fig. 3. Moisture distribution in EGP hollow sphere.

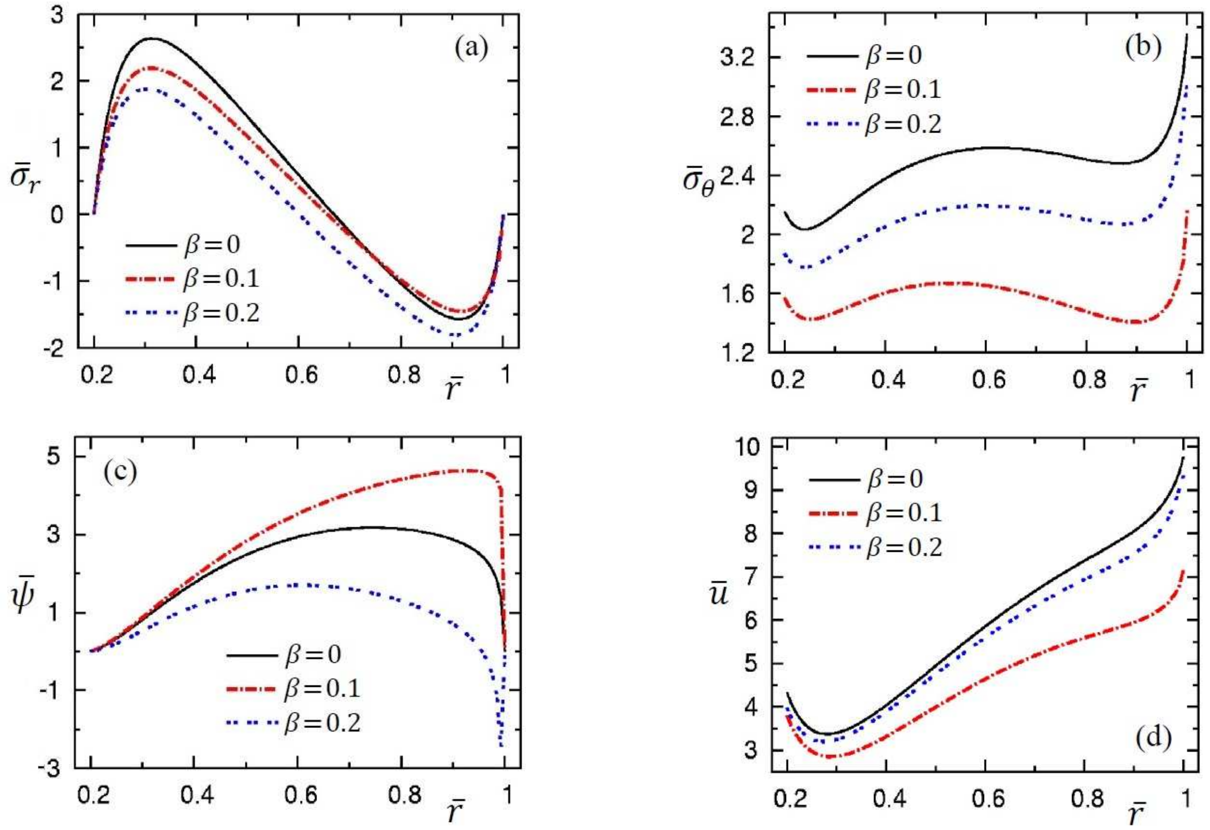

Fig. 4. Stresses, electric potential, and displacement with different porosity factors without electrical and mechanical loads (Case 1).

Numerical outcomes for such perfect or porous hollow spheres are plotted in Figs. 2-11 and reported in Tables 2-5. Figure 2 depicts the temperature distribution for the porous sphere. The temperature decreases along the radial direction and satisfies the boundary conditions. Figure 3 displays moisture concentration along the radial direction of the sphere. The moisture increases along the radial direction of the sphere.

The porosity factor β for the porous sphere is considered in two values $\beta = 0.1$, 0.2 while for the perfect sphere we set $\beta = 0$. The boundary conditions are considered for four different cases of electrical and mechanical loading in the following form:

Case 1: $P_1 = 0$ (Pa), $P_2 = 0$ (Pa), $\psi_1 = 0$ (W/A), $\psi_2 = 0$ (W/A).

Case 2: $P_1 = 10^{10}$ (Pa), $P_2 = 0$ (Pa), $\psi_1 = 0$ (W/A), $\psi_2 = 0$ (W/A).

Case 3: $P_1 = 0$ (Pa), $P_2 = 0$ (Pa), $\psi_1 = 10^8$ (W/A), $\psi_2 = 0$ (W/A).

Case 4: $P_1 = 0$ (Pa), $P_2 = 10^{10}$ (Pa), $\psi_1 = 0$ (W/A), $\psi_2 = 10^8$ (W/A).

5.1 Case 1

Examine a porous sphere without any electrical and mechanical pressures. Here, we take the dimensionless stresses, electric potential, and displacement in the form

$$\{\bar{\sigma}_r, \bar{\sigma}_\theta\} = \{\sigma_r, \sigma_\theta\} \times 10^2 \text{ Pa}, \quad \bar{\psi} = \psi \times 10^2 \text{ W/A}, \quad \bar{u} = \frac{u}{b} \times 10^3.$$

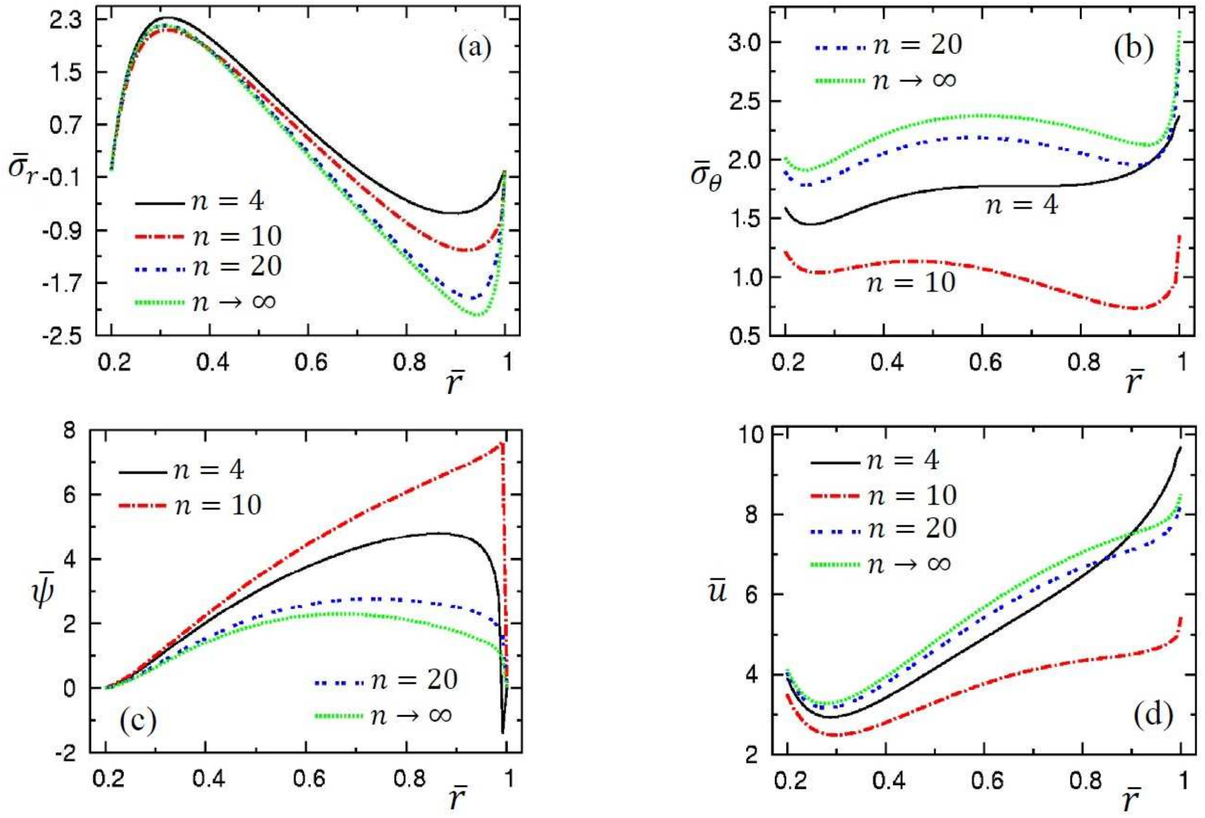

Fig. 5. Stresses, electric potential, and displacement with different grading indexes without electrical and mechanical loads (Case 1).

In Table 2, comparisons between displacement, stresses, and electrical potential for porous and perfect FGP spheres with different grading index n are made. For both spheres, all variables are very sensitive to the variation of the grading index n. The table shows that for the same value of radius parameter $\bar{r}$, the displacement, stresses, and electrical potential values in the porous sphere are less than the corresponding ones in the perfect sphere.

Figures 4 and 5 illustrate the results of Case 1. Figure 4 displays stresses, electrical potential, and displacement of the FGP spheres ($n = 12$) with various values of the porosity factor β. Figure 4(a) corresponds to the radial stress $\bar{\sigma}_r$ for perfect sphere ($\beta = 0$) and porous spheres ($\beta = 0.1, 0.2$). We notice that from $\bar{r} = 0.2$ to $\bar{r} = 0.7$ the value of radial stress for the perfect sphere is greater than the corresponding ones of porous spheres. However, for $\bar{r} = 0.7$ to $\bar{r} = 1$ the radial stress for the perfect sphere intermediates the corresponding ones of the porous sphere. The hoop stress $\bar{\sigma}_\theta$ is exhibited in Fig. 4(b) for various values of β. The hoop stress $\bar{\sigma}_\theta$ in the perfect sphere is greater than the corresponding ones of the porous spheres along the radial direction of the sphere. Fig. 4(c) shows the electrical potential $\bar{\psi}$ for different values of β. The curves are increasing and then decreasing near the outer surface to satisfy the boundary conditions. The electrical potential $\bar{\psi}$ of the perfect sphere intermediates those of the porous sphere. The radial displacements $\bar{u}$ along the composite sphere are demonstrated in Fig. 4(d) with different values of β. The perfect sphere gives the greatest radial displacement.

Figure 5 displays the stresses, electrical potential, and displacement of the FGP porous spheres ($\beta = 0.1$) for various values of grading index n. Figures 5(a) illustrates the highest radial stress $\bar{\sigma}_r$ along the porous sphere for small $n = 4$ and the smallest radial stress $\bar{\sigma}_r$ for $n \to \infty$. This is not the same for the hoop stress $\bar{\sigma}_\theta$ as shown in Fig. 5(b) in which the highest $\bar{\sigma}_\theta$ occurs for $n \to \infty$ while the smallest $\bar{\sigma}_\theta$ occurs for $n = 10$. Figures 5(c) illustrates the highest electrical potential $\bar{\psi}$ along the porous sphere for $n = 10$ and the smallest electrical potential $\bar{\psi}$ for $n \to \infty$. However, Fig. 5(d) shows the highest radial displacement $\bar{u}$ along the porous sphere ($0 \leq \bar{r} < 0.9$) for $n \to \infty$ and the smallest $\bar{u}$ for $n = 10$. In fact, Figures 5(a) and 5(c) satisfy the boundary conditions for mechanical and electrical loading.

Table 2. Effect of porosity factor without electrical and mechanical loads for FGP perfect and porous spheres with different grading index (Case 1).

	$\bar{r}$	Perfect FGPM ($\beta = 0$)			Porous FGPM ($\beta = 0.2$)		
		$n = 5$	$n = 10$	$n = 20$	$n = 5$	$n = 10$	$n = 20$
$\bar{u}$	0.3	3.2181	3.3636	3.4949	2.9818	3.0892	1.9583
	0.5	4.6072	4.8754	5.1215	4.2684	4.4635	2.3710
	0.7	6.2896	6.5684	6.9220	5.7270	5.8969	2.6151
$\bar{\sigma}_r$	0.3	2.6930	2.6336	2.5932	1.9204	1.8947	1.5935
	0.5	1.6435	1.4977	1.3936	0.92175	0.84471	0.72468
	0.7	0.10590	-0.20172	-0.37042	-0.38445	-0.59240	-0.46953
$\bar{\sigma}_\theta$	0.3	1.8529	2.0781	2.2739	1.5449	1.6788	0.59137
	0.5	2.1990	2.4608	2.6946	1.7799	1.9376	0.4969
	0.7	2.2651	2.4971	2.7476	1.7884	1.9145	0.2108
$\bar{\psi}$	0.3	0.9573	0.8399	0.7432	0.6929	0.6209	0.9410
	0.5	3.0360	2.5828	2.2083	2.1903	1.9081	3.2948
	0.7	4.2521	3.3634	2.6298	2.8702	2.3239	5.3758

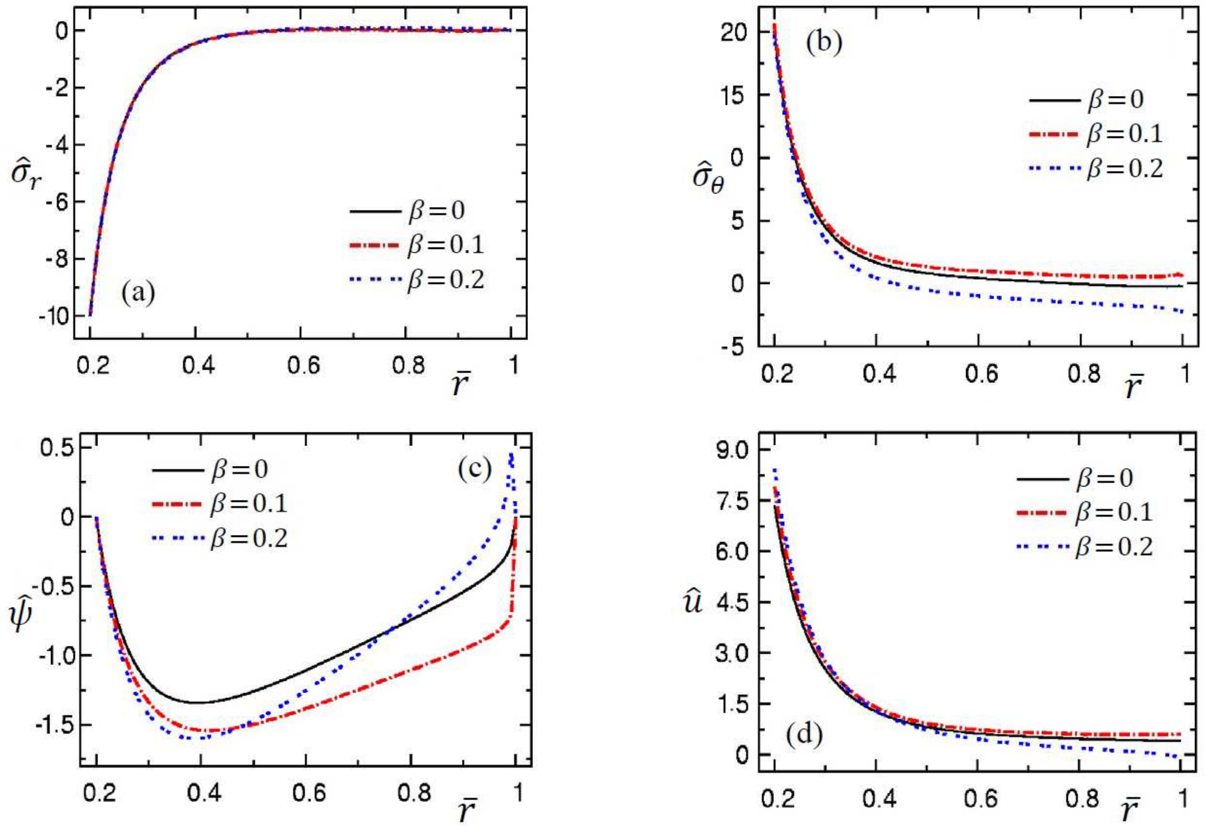

Fig. 6. Stresses, displacement, and electric potential with different porosity factors with mechanical pressure only (Case 2).

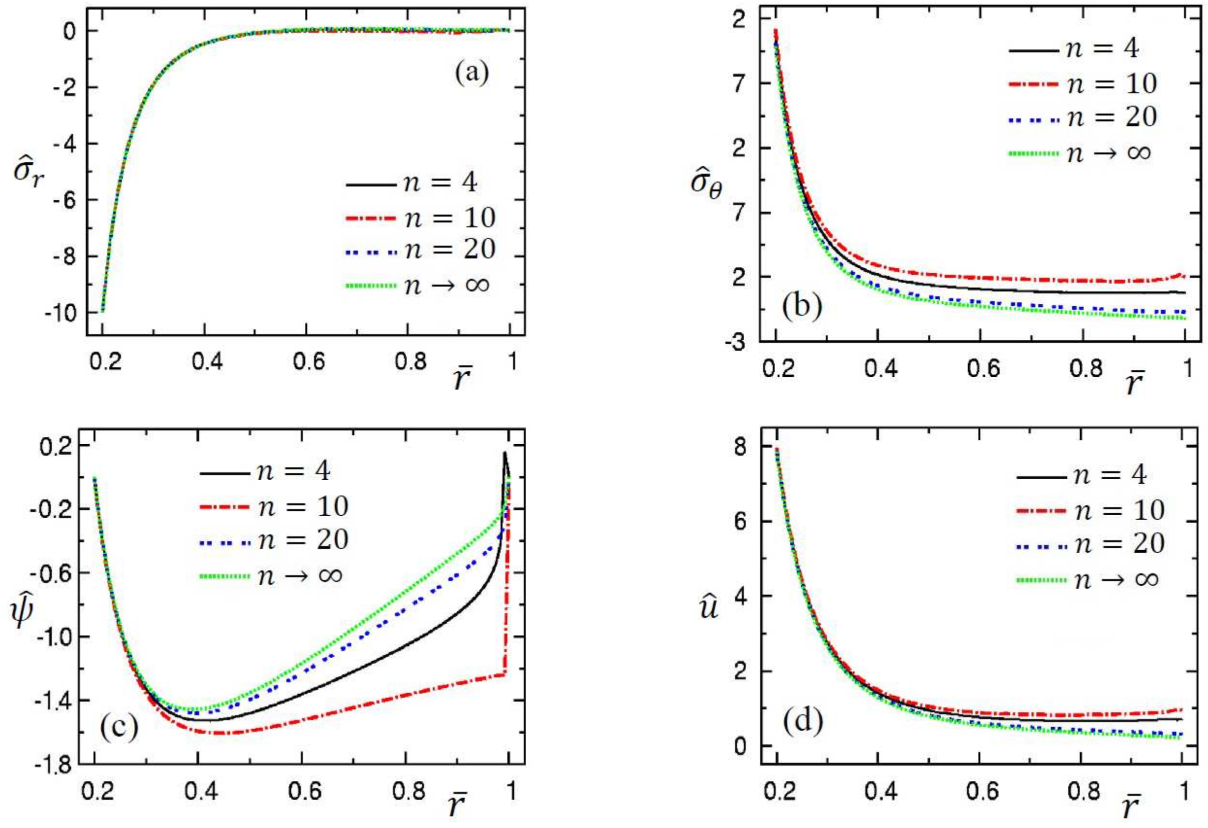

Fig. 7. Stresses, displacement, and electric potential with different grading indexes with mechanical pressure only (Case 2).

Table 3. Effect of porosity factor with mechanical loading for FGP perfect and porous spheres with different grading index (Case 2).

	$\bar{r}$	Perfect FGPM ($\beta = 0$)			Porous FGPM ($\beta = 0.2$)		
		$n = 5$	$n = 10$	$n = 20$	$n = 5$	$n = 10$	$n = 20$
$\hat{u}$	0.3	2.5707	2.5382	2.5141	2.8766	2.8367	3.0770
	0.5	0.89594	0.83682	0.79216	0.87363	0.80129	1.2458
	0.7	0.64841	0.55436	0.48631	0.51610	0.40622	1.1012
$\hat{\sigma}_r$	0.3	-1.8923	-1.9058	-1.9076	-1.9349	-1.9461	-1.8841
	0.5	-0.07200	-0.07854	-0.07304	-0.09140	-0.09308	-0.07047
	0.7	0.02973	0.03388	0.04695	0.04399	0.05751	0.026103
$\hat{\sigma}_\theta$	0.3	4.9158	4.5669	4.2599	4.3014	3.9226	6.2439
	0.5	1.3937	0.92993	0.54299	0.48369	-0.01046	3.0583
	0.7	0.8635	0.3051	-0.1368	-0.14087	-0.71609	2.8987
$\hat{\psi}$	0.3	-1.2053	-1.1979	-1.1864	-1.4586	-1.4479	-1.5174
	0.5	-1.3064	-1.2722	-1.2262	-1.5973	-1.5498	-1.8496
	0.7	-1.0321	-0.9565	-0.8624	-1.2449	-1.1460	-1.8043

5.2 Case 2

For this case, the porous sphere is under an internal pressure P_1 only. In this case the sphere deal like a sensor. The dimensionless variables take the form

$$\hat{\sigma}_r = \frac{\sigma_r}{P_1} \times 10, \quad \hat{\sigma}_\theta = \frac{\sigma_\theta}{P_1} \times 10^2, \quad \hat{\psi} = \psi \times 10\ \mathrm{W/A}, \quad \hat{u} = \frac{u}{b} \times 10^2.$$

The results are reported in Table 3 and Figures 6 and 7 for such cases. Table 3 shows the difference between stresses, electric potential, and displacement at different values of porosity coefficients β and grading index n. It is noted that the numerical values of all variables are very sensitives to the variations of porosity, the FGP parameter, and different positions of the spheres. Figure 6 corresponds to the stresses, electrical potential, and displacement of the FGP perfect and porous spheres ($n = 12$) subjected to internal mechanical pressure only. The radial stress $\hat{\sigma}_r$ is displayed in Fig. 6(a). All curves are coinciding for all values of β. The curves vanish at the outer surface of the sphere in which they achieve the boundary conditions. The maximum value of radial stress $\hat{\sigma}_r$ appears at the outer surface while the minimum value occurs at the inner one. The hoop stress $\hat{\sigma}_\theta$ is presented in Fig. 6(b). It is decreasing along the radial direction of the perfect and porous spheres. The greatest value of hoop stress $\hat{\sigma}_\theta$ occurs at the inner surface of the sphere. The hoop stress $\hat{\sigma}_\theta$ for the perfect sphere intermediates the corresponding ones of the porous sphere. Figure 6(c) shows the electrical potential $\hat{\psi}$ for different values of β. The electrical potential $\hat{\psi}$ is no longer decreasing and increasing to get its highest values at or near the outer surface of the sphere. Positive displacement $\bar{u}$ is depicted in Fig. 6(d). The displacement is decreasing along the radial direction of the sphere.

Figure 7 shows the stresses, electrical potential, and displacement of the FGP porous spheres ($\beta = 0.1$) under internal mechanical pressure only. The radial stress $\hat{\sigma}_r$ displayed in Fig. 7(a) is not sensitive to the variation of the grading index n. Once again, the curves vanish at the outer surface of the porous sphere to achieve the boundary conditions. The hoop stress $\hat{\sigma}_\theta$ is presented in Fig. 7(b). It is decreasing along the radial direction of the porous sphere. The greatest value of hoop stress $\hat{\sigma}_\theta$ occurs when $n = 10$ while the smallest one occurs when $n \to \infty$. Figure 7(c) shows the electrical potential $\hat{\psi}$ for distinct values of the grading index n. The electrical potential $\hat{\psi}$ is no longer decreasing and increasing to get its highest values at or near the outer surface of the porous sphere. Positive displacement $\hat{u}$ is depicted in Fig. 7(d). The displacement is decreasing along the radial direction of the sphere. The highest value of $\hat{\psi}$ occurs when $n \to \infty$ while the smallest $\hat{\psi}$ occurs when $n = 10$. The inverse of this phenomenon is shown for the radial displacement $\hat{u}$ in Fig. 7(d).

5.3 Case 3

The composite sphere is influenced by a constant voltage and free mechanical loading at the inner surface and grounded without any mechanical pressure at the outer surface. Here, the sphere behavior is represented as an actuator. The dimensionless variables are

$$\breve{\sigma}_r = \sigma_r \times 10^2\ \mathrm{Pa}, \quad \breve{\sigma}_\theta = \sigma_\theta \times 10\ \mathrm{Pa}, \quad \breve{\psi} = \frac{\psi}{\psi_1}, \quad \breve{u} = \frac{u}{b} \times 10^2.$$

Results for this case are reported in Table 4 and displayed in Figs. 8 and 9. In Table 4, the results for all variables are very sensitive to the variations in porosity factor, grading index, and for different positions in the perfect and porous spheres. Figure 8 clarifies the stresses, electric potential, and radial displacement of the FGP spheres ($n = 12$) for various values of porosity factor β. This figure explains the results with pure internal electric potential.

The radial stress is displayed in Figure 8(a) without mechanical pressure on inner and outer surfaces. It is shown that the radial stress $\breve{\sigma}_r$ vanishes on the inner and outer surfaces of the perfect and porous spheres which satisfies the boundary conditions of the case. The porosity factor $\beta = 0.2$ yields the smallest radial stress $\breve{\sigma}_r$. Figure 8(b) presents the hoop stress $\breve{\sigma}_\theta$ of the perfect and porous spheres. The hoop stress $\breve{\sigma}_\theta$ is monotonically increasing along the radial direction of the sphere. The greatest value of $\breve{\sigma}_\theta$ exists at the outer surface. The maximum value of $\breve{\sigma}_\theta$ occurs at $\beta = 0.2$ and the minimum value occurs at $\beta = 0.1$. So, we can conclude that for porous sphere the hoop stress increase with increasing the porosity factor β. Also, the perfect sphere yields hoop stress $\breve{\sigma}_\theta$ included in those of the porous spheres.

Figure 8(c) demonstrate the electric potential $\breve{\psi}$ of the FGP perfect and porous spheres for different values of porosity factor β. The electric potential $\breve{\psi} = 1$ at the inner surface of the sphere and vanishes at the outer surface to meet the boundary conditions. The maximum values of $\breve{\psi}$ occur when $\beta = 0.1$ while the minimum values occur when $\beta = 0.2$. So, we can conclude that for porous sphere the electric potential $\breve{\psi}$ increases with the decrease in porosity factor β. Also, the perfect sphere yields electric potential $\breve{\psi}$ included in those of the porous spheres. The radial displacement $\breve{u}$ is presented in Fig. 8(d). The displacement increases along the radial direction of the sphere. The maximum values of $\breve{u}$ occur when $\beta = 0.2$ while the minimum values occur when $\beta = 0.1$. That means that the radial displacement $\breve{u}$ of porous sphere increases as the porosity factor β increases. Also, the perfect sphere yields radial displacement $\breve{u}$ included in those of the porous spheres.

Figure 9 shows the stresses, electrical potential, and displacement of the FGP porous spheres ($\beta = 0.1$) subjected to internal electrical potential only. The radial stress $\breve{\sigma}_r$ displayed in Fig. 9(a) is very sensitive to the variation of the grading index n. Once again, the curves vanish at the inner and outer surfaces of the porous sphere to achieve the boundary conditions. The highest values of $\breve{\sigma}_r$ occur when $n = 4$. The hoop stress $\breve{\sigma}_\theta$ is presented in Fig. 9(b). The smallest value of hoop stress $\breve{\sigma}_\theta$ occurs when $n = 10$ while the greatest one occurs when $n \to \infty$.

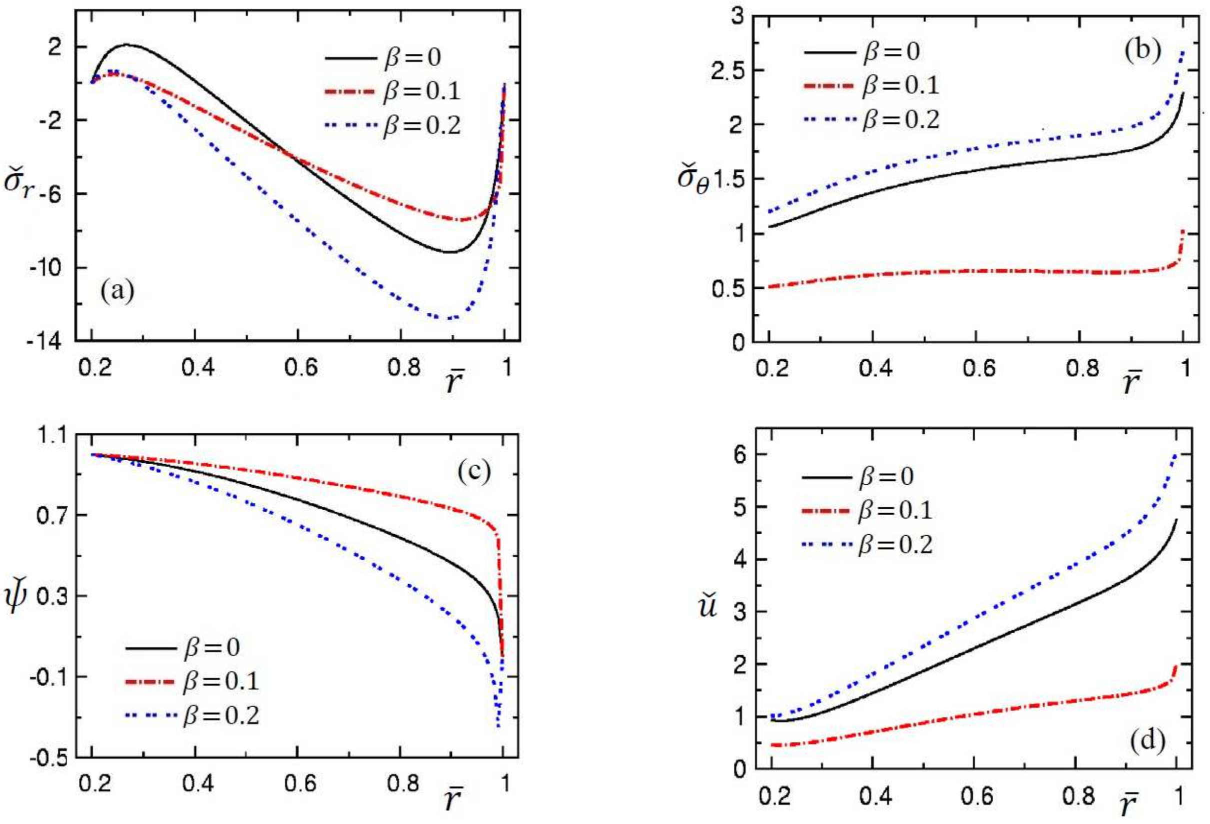

Fig. 8. Stresses, displacement, and electric potential with different porosity factors with electric loading (Case 3).

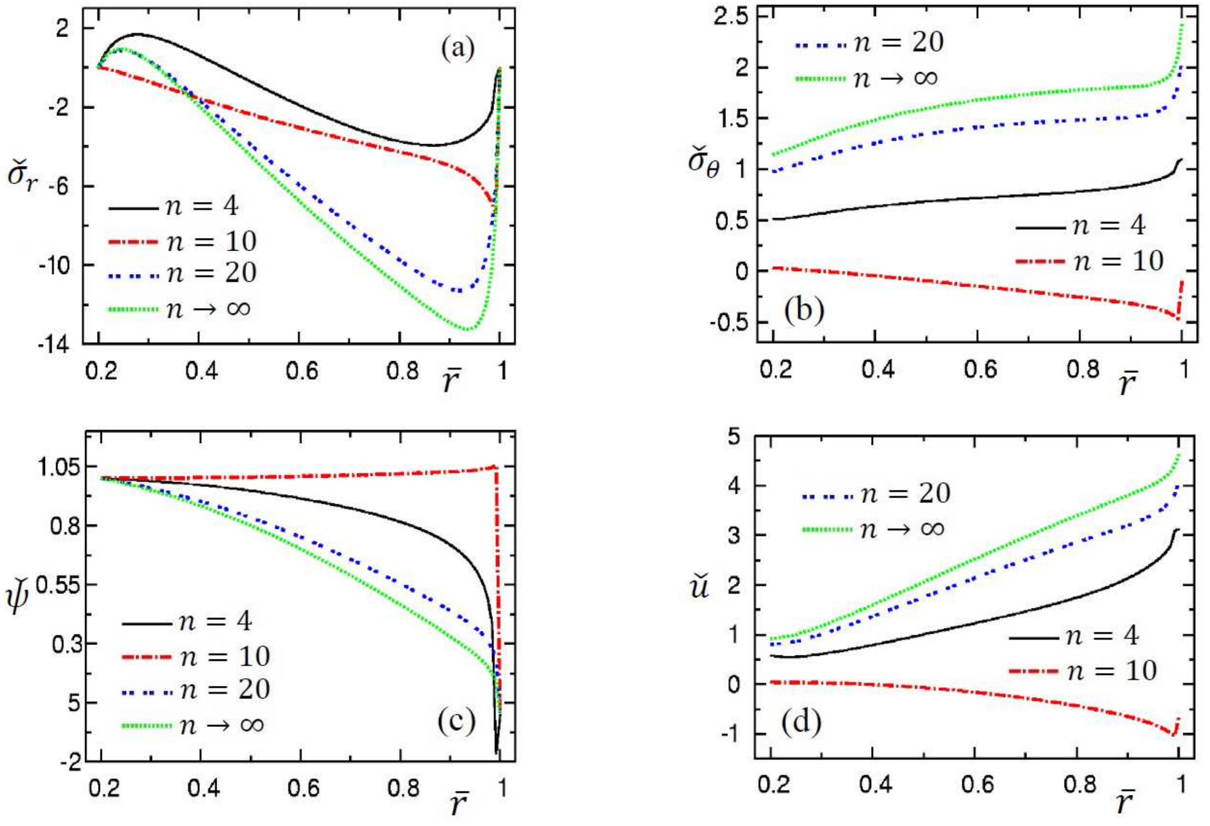

Fig. 9. Stresses, displacement, and electric potential with different grading indexes with electric loading (Case 3).

Figure 9(c) shows the electrical potential $\breve{\psi}$ of the porous sphere for various values of the grading index n. The electrical potential $\breve{\psi}$ is very sensitive to the variation in the grading index n. The radial displacement $\breve{u}$ is depicted in Fig. 9(d). The displacement is decreasing along the radial direction of the sphere only for $n = 10$. The highest value of $\breve{u}$ occurs when $n \to \infty$ while the smallest $\breve{u}$ occurs when $n = 10$. The inverse of this phenomena is shown for the electrical potential $\breve{\psi}$ in Fig. 9(c).

Table 4. Effect of porosity factor with mechanical loading for FGP perfect and porous spheres with different grading index (Case 3).

	$\bar{r}$	Perfect FGPM ($\beta = 0$)			Porous FGPM ($\beta = 0.2$)		
		$n = 5$	$n = 10$	$n = 20$	$n = 5$	$n = 10$	$n = 20$
	0.3	0.79473	1.0199	1.2146	0.89213	1.0805	-0.60330
$\breve{u}$	0.5	1.3423	1.7621	2.1263	1.5439	1.8952	-1.2193
	0.7	1.9829	2.5681	3.1037	2.2572	2.7281	-2.1514
	0.3	2.5323	2.0374	1.6219	0.6531	0.2276	-4.3584
$\breve{\sigma}_r$	0.5	-0.1705	-1.6841	-2.9570	-2.6911	-3.8961	-5.8318
	0.7	-3.1458	-5.7158	-7.7516	-5.8039	-7.8649	-6.0737
	0.3	0.81624	1.1407	1.4203	0.88729	1.1210	-0.49222
$\breve{\sigma}_\theta$	0.5	1.0034	1.3944	1.7326	1.0649	1.3459	-0.79421
	0.7	1.1178	1.5364	1.9082	1.1676	1.4630	-1.0646
	0.3	0.98378	0.96858	0.95555	0.96829	0.95583	1.0027
$\breve{\psi}$	0.5	0.92753	0.86839	0.81747	0.87032	0.82209	1.0256
	0.7	0.83002	0.71731	0.61690	0.72141	0.63277	1.0825

5.4 Case 4

The fourth case is the merging of the second and third cases together. In this case the FGP composite sphere influence by mechanical pressure and constant electric potential on the outer surface but on the inner surface, there is no mechanical pressure and grounded electric potential. The numerical results are plotted in Figures 10 and 11 and reported in Table 5. The dimensionless stresses, electric potential, and displacement are given by:

$$\tilde{\sigma}_r = \frac{\sigma_r}{P_2}, \quad \tilde{\sigma}_\theta = \frac{\sigma_\theta}{P_2}, \quad \tilde{\psi} = \frac{\psi}{\psi_2}, \quad \tilde{u} = \frac{u}{b} \times 10^2.$$

In Table 5 the numerical values of displacement, stresses, and electric potential in the perfect and porous sphere are greater than those of the perfect sphere when $n = 5$, $n = 20$, and for different values of β. In the case of $n = 10$ the numerical values of the porous sphere are less than those of the perfect sphere.

Figure 10(a) depicts the radial stress $\tilde{\sigma}_r$ of the FGP perfect and porous spheres ($n = 12$) for different values of β. By increasing the porosity factor β the radial stress increases. The hoop stress $\tilde{\sigma}_\theta$ is displayed in Fig. 10(b). The hoop stress decreases along the radial direction of the sphere and has a maximum value at the inner surface. The electric potential $\tilde{\psi}$ is shown in Fig. 10(c) in which it is satisfying the boundary conditions. Figure 10(d) shows that the radial displacement $\tilde{u}$ decreases along the radius of the perfect and porous spheres and has the maximum values when $\beta = 0.1$. The perfect sphere yields $\tilde{\psi}$ and $\tilde{u}$ intermediate those of the porous spheres.

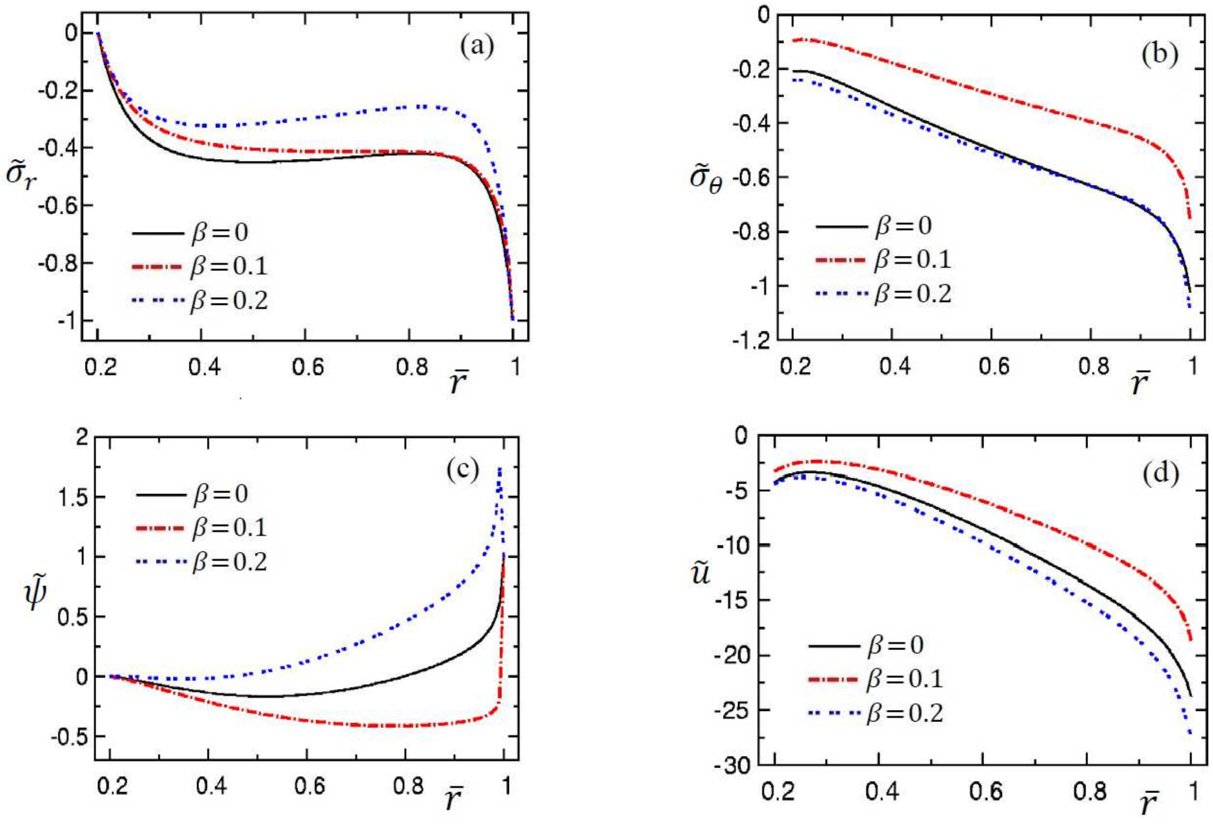

Fig. 10. Stresses, displacement, and electric potential with different porosity factors with electric and mechanical loading (Case 4).

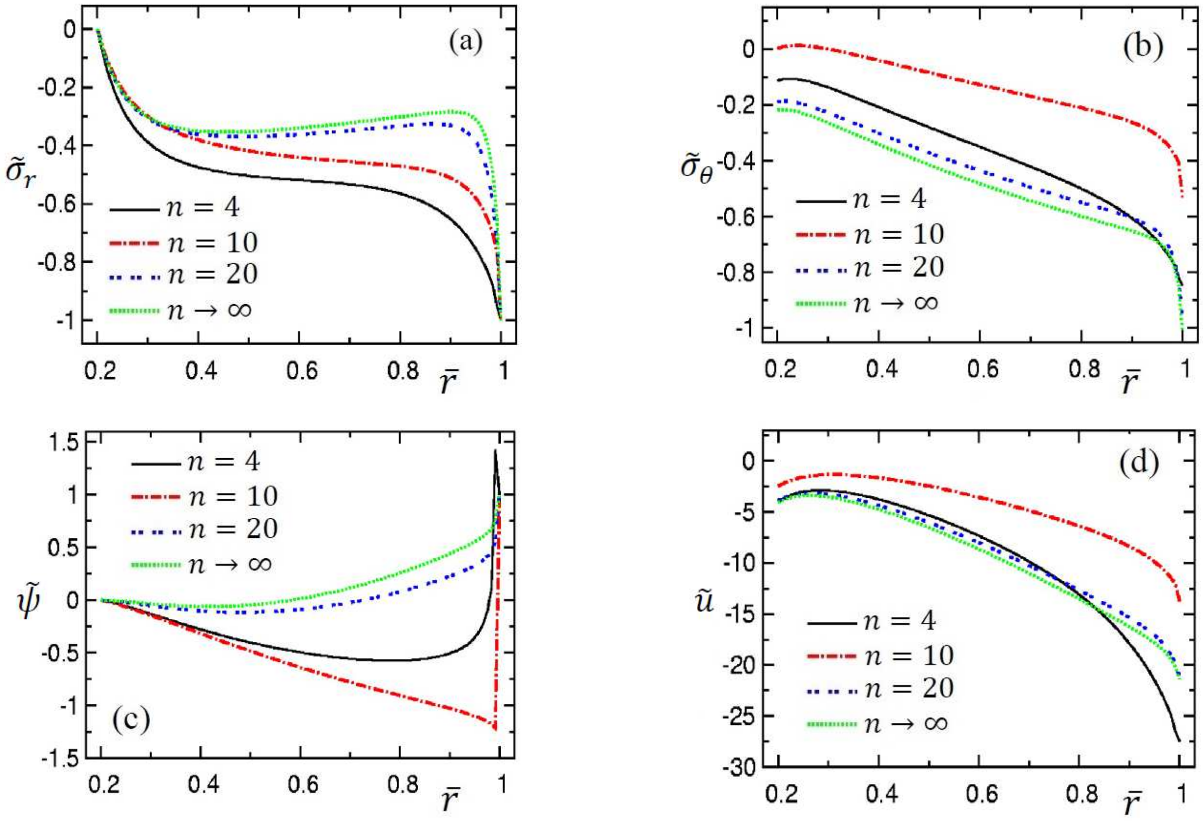

Fig. 11. Stresses, displacement, and electric potential with different grading indexes with electric and mechanical loading (Case 4).

Figure 11 shows the stresses, electrical potential, and displacement of the FGP porous spheres ($\beta = 0.1$) subjected to external mechanical pressure and electrical potential. The radial stress $\tilde{\sigma}_r$ displayed in Fig. 11(a) is very sensitive to the variation of the grading index n. Once again, the curves vanish at the inner surface only of the porous sphere to achieve the boundary conditions. The highest values of $\tilde{\sigma}_r$ occur when $n \to \infty$ while the smallest values of $\tilde{\sigma}_r$ occur when $n = 4$. The hoop stress $\tilde{\sigma}_\theta$ is presented in Fig. 11(b). The smallest value of hoop stress $\tilde{\sigma}_\theta$ occurs when $n \to \infty$ while the greatest one occurs when $n = 10$.

Figure 11(c) shows the electrical potential $\tilde{\psi}$ of the porous sphere for various values of the grading index n. The electrical potential $\tilde{\psi}$ is very sensitive to the variation in the grading index n. The radial displacement $\tilde{u}$ is depicted in Fig. 11(d). The displacement is decreasing along the radial direction of the sphere. The highest value of $\tilde{u}$ occurs when $n = 10$ while the smallest $\tilde{u}$ occurs when $n \to \infty$ in the interval $0.2 \le \bar{r} < 0.8$. The inverse of this phenomenon is shown for the electrical potential $\tilde{\psi}$ in Fig. 11(c).

6. Conclusions

This research discussed the effect of the porosity factor and hygrothermal parameters on a hollow sphere. Four different cases are presented. In such cases, the sphere may be affected by mechanical pressures or/and electric potential. Through the results and discussion, we can conclude that:

- In all cases, all variables of the studied sphere are very sensitive to the variation of the grading index n.
- By choosing suitable values for the porosity parameter we obtain expected values for stresses, displacement, and electric potential.
- The semi-analytical solution method is effective for reaching specific stresses in the perfect and porous spheres.
- The studied geometric model of the FGP sphere in the presence of porosity coefficient and different loads is possible to control the values of the resulting stresses and displacements.

Table 5. Effect of porosity factor with electrical and mechanical loading for FGP perfect and porous spheres with different grading index (Case 4).

	$\bar{r}$	Perfect FGPM ($\beta = 0$)			Porous FGPM ($\beta = 0.2$)		
		$n = 5$	$n = 10$	$n = 20$	$n = 5$	$n = 10$	$n = 20$
$\tilde{u}$	0.3	-3.1742	-3.4195	-3.6601	-3.4860	-3.5733	-0.0416
	0.5	-5.8080	-6.2780	-6.7391	-6.4427	-6.6153	-0.0886
	0.7	-10.385	-10.778	-11.386	-11.339	-11.216	-0.9430
$\tilde{\sigma}_r$	0.3	-0.41739	-0.37843	-0.35303	-0.33063	-0.29497	-0.18780
	0.5	-0.53145	-0.46414	-0.41812	-0.40378	-0.34706	-0.29007
	0.7	-0.54756	-0.45087	-0.38962	-0.40298	-0.32246	-0.34025
$\tilde{\sigma}_\theta$	0.3	-0.18691	-0.24148	-0.28763	-0.20708	-0.23701	0.09513
	0.5	-0.34871	-0.40633	-0.45738	-0.35147	-0.37934	0.06454
	0.7	-0.50084	-0.55033	-0.60179	-0.48555	-0.50174	0.02559
$\tilde{\psi}$	0.3	-0.11957	-0.07946	-0.04912	-0.07683	-0.04524	-0.13518
	0.5	-0.34821	-0.19967	-0.08623	-0.20001	-0.08468	-0.48154
	0.7	-0.43568	-0.15986	0.0537	-0.1611	0.0425	-0.84686

Author Contributions

All authors initiated the paper and suggested the mathematical method. The manuscript was written through the contribution of all authors. They discussed the results, reviewed and approved the final version of the manuscript.

Acknowledgments

Not applicable.

Conflict of Interest

The authors declared no conflict of interest.

Funding

The authors received no financial support for the research, authorship, and publication of this article.

Data Availability Statements

The datasets generated and/or analyzed during the current study are available from the corresponding author on reasonable request.

Nomenclature

a	Inner radii of the sphere [m]	$\alpha_i\ (i=r,\theta)$	Thermal expansion coefficients [K^{-1}]
b	Outer radii of the sphere [m]	β	A porosity volume function
$C(r)$	Moisture concentration	$c_{ij}\ (i=r,\theta, j=r,\theta,\varphi)$	Elastic coefficients [Pa]
D_r	Electric displacement	$e_{rj}\ (j=r,\theta)$	Piezoelectric parameters [Cm^{-2}]
$\eta_i\ (i=r,\theta)$	Moisture expansion coefficients [$\mathrm{m}^3\mathrm{kg}^{-1}\mathrm{Pa}$]	ε_{rr}	Dielectric parameters [$\mathrm{C}^2\mathrm{K}^{-1}\mathrm{m}^2$]
ψ	Electric potential distribution [W/A]	K	Mean of thermal conductivity [W/K m]
n	Grading index	$r^{(k)}$	Mean radius of the kth subdomain [m]
$s^{(k)}$	Radial width of the kth subdomain [m]	σ_r	Radial stress distribution [Pa]
σ_θ	Circumferential stress distribution [Pa]	$T(r)$	Temperature distribution [K]
T_0	Reference initial temperature [K]	p_a	Properties of the inner surface
p_b	Properties of the outer surface	p_{11}	Pyroelectric coefficients [$\mathrm{CK}^{-1}\mathrm{m}^{-2}$]
p_{22}	Hygroelectric coefficients [$\mathrm{CK}^{-1}\mathrm{m}^{-2}$]	P_1	Inner pressure [Pa]
P_2	Outer pressure [Pa]	$u(r)$	Radial displacement [m]
Q	Constant rate of internal energy generation [$\mathrm{W/m}^3$]	$q(r)$	Heat generation function [K]

References

[1] Zhang, Y., Wang, J., Fabrication of functionally graded porous polymer structures using thermal bonding lamination techniques, *Procedia Manufacturing*, 10, 2017, 866–875.

[2] Wang, Y., Wan, Y., Zhang, Y., Vibrations of longitudinally traveling functionally graded material plates with porosities, *European Journal of Mechanics - A/Solids*, 66, 2017, 55–68.

[3] Gupta, A., Talha, M., Influence of initial geometric imperfections and porosity on the stability of functionally graded material plates, *Mechanics Based Design of Structures and Machines*, 46, 2017, 693–711.

[4] Zhou, K., Lin, Z., Huang, X., Hua, H., Vibration and sound radiation analysis of temperature-dependent porous functionally graded material plates with general boundary conditions, *Applied Acoustics*, 154, 2019, 236–250.

[5] Akbas, S., Thermal effects on the vibration of functionally graded deep beams with porosity, *International Journal of Applied Mechanics*, 9(5), 2017, 1750076.

[6] Daikh, A.A., Zenkour, A.M., Free vibration and buckling of porous power law and sigmoid functionally graded sandwich plates using a simple higher order shear deformation theory, *Materials Research Express*, 6, 2019, 115707.

[7] Barati, M.R., Sadr, M.H., Zenkour, A.M., Buckling analysis of higher order graded smart piezoelectric plates with porosities resting on elastic foundation, *International Journal of Mechanical Sciences*, 117, 2016, 309–320.

[8] Zenkour, A.M., A quasi-3D refined theory for functionally graded single layered and sandwich plates with porosities, *Composite Structures*, 201, 2018, 36–48.

[9] Sobhy, M., Zenkour, A.M., Porosity and inhomogeneity effects on the buckling and vibration of double FGM nanoplates via a quasi-3D refined theory, *Composite Structures*, 220, 2019, 289–303.

[10] Zenkour, A.M., Radwan, A.F., Bending response of FG plates resting on elastic foundations in hygrothermal environment with porosities, *Composite Structures*, 213, 2019, 133–143.

[11] Jabbari, M., Karampour, S., Eslami, M.R., Steady state thermal and mechanical stresses of a poro-piezo FGM hollow sphere, *Meccanica*, 48, 2013, 699–719.

[12] Barati, M.R., Zenkour, A.M., Electro-thermoelastic vibration of plates made of porous functionally graded piezoelectric materials under various boundary conditions, *Journal of Vibration and Control*, 24(10), 2016, 1910–1926.

[13] Zenkour, A.M., Aljadani, M.H., Porosity effect on thermal buckling behavior of actuated functionally graded piezoelectric nanoplates, *European Journal of Mechanics/A Solids*, 78, 2019, 103835.

[14] Allam, M.N.M., Tantawy, R., Thermomagnetic viscoelastic responses in a functionally graded hollow structure, *Acta Mechanica Sinica*, 27(4), 2011, 567–577.

[15] Dai, H.L., Hong, L., Fu, Y.M., Xiao, X., Analytical solution for electro magneto thermoelastic behaviors of a functionally graded piezoelectric hollow cylinder, *Applied Mathematical Modelling*, 34, 2010, 343–357.

[16] Allam, M.N.M., Tantawy, R., Zenkour, A.M., Magneto-thermo-elastic response of exponentially graded piezoelectric hollow spheres, *Advances in Computational Design*, 3, 2018, 303–318.

[17] Dai, H.L., Xiao, X., Fu, Y.M., Analytical solutions of stresses in functionally graded piezoelectric hollow structures, *Solid State Communications*, 150, 2010, 763–767.

[18] Reddy, J.N., Chin, C.D., Thermomechanical analysis of functionally graded cylinders and plates, *Journal of Thermal Stresses*, 21, 1998, 593–626.

[19] Reddy, J.N., Analysis of functionally graded plates, *International Journal for Numerical Methods in Engineering*, 47, 2000, 663–684.

[20] Reddy, J.N., Cheng, Z.Q., Three-dimensional thermomechanical deformations of functionally graded rectangular plates, *European Journal of Mechanics - A/Solids*, 20, 2001, 841–855.
[21] Zenkour, A.M., A comprehensive analysis of functionally graded sandwich plates: Part 1 Deflection and stresses, *International Journal of Solids and Structures*, 42, 2005, 5224–5242.
[22] Zenkour, A.M., A comprehensive analysis of functionally graded sandwich plates: Part 2 Buckling and free vibration, *International Journal of Solids and Structures*, 42, 2005, 5243–5258.
[23] Zenkour, A.M., Generalized shear deformation theory for bending analysis of functionally graded plates, *Applied Mathematical Modelling*, 30, 2006, 67–84.
[24] Allam, M. N. M., Zenkour, A.M., Tantawy, R., Analysis of functionally graded piezoelectric cylinders in a hygrothermal environment, *Advances in Applied Mathematics and Mechanics*, 6, 2014, 233-246.
[25] Allam, M.N.M., Tantawy, R., Yousof, A., Zenkour, A.M., Elastic and viscoelastic stresses of nonlinear rotating functionally graded solid and annular disks with gradually varying thickness, *Archive of Mechanical Engineering*, 4, 2017, 423–440.
[26] Sankar, B.V., An elasticity solution for functionally graded beams, *Composites Science and Technology*, 61, 2001, 689–696.
[27] Zenkour, A.M., Benchmark trigonometric and 3-D elasticity solutions for an exponentially graded thick rectangular plate, *Archive of Applied Mechanics*, 77, 2007, 197–214.
[28] Zenkour, A.M., Elsibai, K.A., Mashat, D.S., Elastic and viscoelastic solutions to rotating functionally graded hollow and solid cylinders, *Applied Mathematics and Mechanics (English Edition)*, 29(12), 2008, 1601–1616.
[29] Cuong, L. T., Nguyen, D. K., Nguyen, N., Khatir, S., Xuan, H. N., Abdel-Wahab, M., A three-dimensional solution for free vibration and buckling of annular plate, conical, cylinder and cylindrical shell of FG porous-cellular materials using IGA, *Composite Structures*, 259, 2021, 113216.
[30] Nguyen, H. X., Nguyen, T. N., Abdel-Wahab, M., Bordas, S.P.A., Xuan, H.N., Vo, T. P., A refined quasi-3D isogeometric analysis for functionally graded microplates based on the modified couple stress theory, *Computer Methods in Applied Mechanics and Engineering*, 313, 2017, 904-940.
[31] Praveen, G.N., Reddy, J.N., Nonlinear transient thermoelastic analysis of functionally graded ceramic–metal plates, *International Journal of Solids and Structures*, 35, 1998, 4457–4476.
[32] Zenkour, A.M., Alghamdi, N.A., Thermoelastic bending analysis of functionally graded sandwich plates, *Journal of Materials Science*, 43, 2008, 2574–2589.
[33] Van, P.P., Thai, C. H., Xuan, H.N., Abdel Wahab, M., Porosity-dependent nonlinear transient responses of functionally graded nanoplates using isogeometric analysis, *Composites Part B: Engineering*, 164, 2019, 215-225.
[34] Allam, M.N.M., Tantawy, R., Zenkour, A.M., Thermoelastic stresses in functionally graded rotating annular disks with variable thickness, *Journal of Theoretical and Applied Mechanics*, 56(4), 2018, 1029–1041.
[35] Li, X.Y., Ding, H.J., Chen, W.Q., Axisymmetric elasticity solutions for a uniformly loaded annular plate of transversely isotropic functionally graded materials, *Acta Mechanica*, 196, 2008, 139–159.
[36] Ueda, S., A cracked functionally graded piezoelectric material strip under transient thermal loading, *Acta Mechanica*, 199, 2008, 53–70.
[37] Thanh, C. L., Nguyen, T. N., Vu, T. H., Khatir, S., Abdel-Wahab, M., A geometrically nonlinear size-dependent hypothesis for porous functionally graded micro-plate, *Engineering with Computers*, 2020, DOI: 10.1007/s00366-020-01154-0.
[38] Heyliger, P., A note on the static behavior of simply-supported laminated piezoelectric cylinders, *International Journal of Solids and Structures*, 34, 1997, 3781–3794.
[39] Bayat, M., Saleem, M., Sahari, B.B., Hamouda, A.M.S., Mahdi, E., Analysis of functionally graded rotating disks of variable thickness, *Mechanics Research Communications*, 35, 2008, 283–309.
[40] Dunn, M.L., Taya, M., Electrostatic field concentrations in and around inhomogenities in piezo-electric solids, *Journal of Applied Mechanics*, 61, 1994, 474–475.
[41] Ghorbanpour Arani, A., Kolahchi, R., Mosallaie Barzoki, A. A., Effect of material in-homogeneity on electro-thermo-mechanical behaviors of functionally graded piezoelectric rotating shaft, *Applied Mathematical Modelling*, 35, 2011, 2771–2789.
[42] Sinha, D.K., Note on the radial deformation of a piezoelectric polarized spherical shell with symmetrical temperature distribution, *Journal of the Acoustical Society of America*, 34, 1962, 1073–1075.
[43] Dai, H.L., Wang, X., Thermo-electro-elastic transient responses in piezoelectric hollow structures, *International Journal of Solids and Structures*, 42, 2005, 1151–1171.
[44] Raja, S., Sinha, P.K., Prathap, G., Dwarakanathan, D., Influence of active stiffening on dynamic behavior of piezo-hygro-thermo elastic composite plates and shell, *Journal of Sound and Vibration*, 278, 2004, 257–283.
[45] Sih, G.C., Michopoulos, J.G., Chou, S.C., *Hygrothermoelasticity*, Dordrecht, Martinus Nijhoff Publisheres, 1986.
[46] Paria, G., Magneto-elasticity and magneto-thermo-elasticity, *Advances in Applied Mechanics*, 10(1), 1967, 73–112.
[47] Ootao, Y., Tanigawa, Y., Transient piezothermoelastic analysis for a functionally graded thermopiezoelectric hollow sphere, *Composite Structures*, 81, 2007, 540–549.
[48] Ghorbanpour Arani, A., Kolahchi, R., Mosallaie Barzoki, A. A., Loghman, A., Electro-thermo-mechanical behaviors of FGPM spheres using analytical method and ANSYS software, *Applied Mathematical Modelling*, 36, 2012, 139–157.

ORCID iD

Rania Tantawy https://orcid.org/0000-0002-0576-2798
Ashraf M. Zenkour https://orcid.org/0000-0002-0883-8073

How to cite this article: Tantawy R., Zenkour A.M. Effect of Porosity and Hygrothermal Environment on FGP Hollow Spheres under Electromechanical Loads, *J. Appl. Comput. Mech.*, 8(2), 2022, 710–722. https://doi.org/10.22055/JACM.2021.39229.3377